Simulation of the deposit evolution on a fan blade for tunnel ventilation

Alessio Castorrini,
Ph.D,
Department of Mechanical and Aerospace Engineering,
Sapienza University of Rome,
Via Eudossiana, 18, I-00184 Rome, Italy
Email: alessio.castorrini@uniroma1.it

Paolo Venturini,
Ph.D,
Department of Mechanical and Aerospace Engineering,
Sapienza University of Rome,
Via Eudossiana, 18, I-00184 Rome, Italy
Email: paolo.venturini@uniroma1.it

Alessandro Corsini,
Professor,
Department of Mechanical and Aerospace Engineering,
Sapienza University of Rome,
Via Eudossiana, 18, I-00184 Rome, Italy
Email: alessandro.corsini@uniroma1.it

Franco Rispoli
Professor,
Department of Mechanical and Aerospace Engineering,
Sapienza University of Rome,
Via Eudossiana, 18, I-00184 Rome, Italy
Email: franco.rispoli@uniroma1.it

ABSTRACT

Fans used in tunnel ventilation operate for decades in an atmosphere that carries dust, soot, and other solid particles. The formation of deposit on the rotor blades, considering a so long time of exposition to this particle-laden flow, is highly probable. A not negligible quantity of deposited material can produce damages on the performance of the fan, but also mass unbalancing, which is potentially dangerous for the structural integrity of the fan components.

We applied our simulation tool to study a case of deposition on a large axial fan blade, used for tunnel ventilation. The outcome of the study is a parametric map of fouled blade geometries, obtained by simulating the deposition process over the increasing quantity of ingested particles mixture. The final map correlates the level and shape of deposit to the overall amount of particle ingested by the fan in its operating life. The same map can be easily used to predict the time needed in a specific application to reach any specific deposit thickness.

The evolution algorithm and simulation tools developed in the past years by the authors was applied to predict the modified geometry of eroded rotor blades. Here the same framework is updated to simulate the deposit problem. We use an integrated multiphase solver, coupled with a geometry update method. The solver can iteratively simulate the flow field, compute the particle tracking, dispersion and deposit processes, and modify the geometry (and mesh) according to the predicted deposit shape and rate.

INTRODUCTION

Large fans are generally used in the ventilation of road and rail tunnels. These fans process a particle-laden airflow, for their entire operative life, which generally extends over several years (20 years is an applicable lifetime [1]). In the specific case of road tunnels, the particulate can be composed of dust, sand, soot, powders from braking systems and tires. Some of these particles can stick to the surface of the blades, generating a layer of deposit, which grows during the years, reducing the fan performances and unbalancing its mass.

Scientific literature about the fans for industrial applications (i.e., induced-draft fans, centrifugal fans, fans for tunnel ventilation, etc.) is limited, especially if talking about the simulation of particle deposition. A wide review of the computational methods that can be adopted in industrial fans is reported in [2]. The authors of this paper started a series of numerical studies on industrial fans ranging from the aerodynamics aspects to erosion prediction (see for instance [1]-[8]). Wang et al. in [9] performed an experimental campaign to measure fouling in an induced-draft fan of a coal power plant. Van Der Spuy and co-workers analysed especially axial flow fan using both CFD and experiments (i.e., [10]-[12]).

The study and numerical prediction of fouling in industrial fans seem to be neglected so far. However, fouling may reduce the performance especially in those applications in which the fan has scarce (if not completely absent) maintenance operations (i.e., fans used in road and metro tunnel ventilation). In order to simulate particle deposition process, hence we have to refer to what was done in other turbomachinery applications. Particle deposition models were largely studied especially for gas turbine and compressors. For instance, Bons and co-workers performed a series of experimental and numerical campaigns in order to predict deposit formation on gas turbine blades, and internal cooling channels ([13]-[15] just to cite few of the most recent). Tafti studied particle impact and adhesion on blade turbines ([16]-[18]). In [19] and [20] particle deposition in impinging jets is studied. Pinelli and co-workers focused their attention especially on the study of compressor fouling ([21],[22]). The authors of the present study also analysed particle deposition on both external and internal turbine and compressor blade surfaces (se for instance [8],[23]-[26]). Particle deposition model in industrial fan applications can be borrowed and adapted from these studies.

Another aspect that should be considered in surface fouling is that, a part from the initial phase, the deposit layer grows and then it interacts with the flow field. While up to few years ago the time evolution of deposit has been neglected in numerical simulations, because it is too expensive in terms of computational cost, now there is an increasing interest in simulating this aspect. For example, some of the cited works ([13],[19],[21]) account for the time evolution of deposit by re-meshing the domain at each particle deposition. Despite this is a very accurate approach, the computational time required to simulate a blade aging process is too high. Having this in mind and considering the industry need of having accurate but also fast computational tools to perform numerical simulations, in 2016 we started developing and optimizing an algorithm to perform long-term predictions whit a short computational time ([3],[4],[27]).

In the present work, we focus on a large axial fan blade, supposing its installation in a road tunnel. The main goal is to reproduce the possible evolution of the deposit pattern on the blade and its effect on the fan performance. Because of the large range of operating conditions at which the fan can work during its life, we made for this study a simplification. Therefore, we will evaluate here the deposition pattern related to the nominal working condition of the fan.

The deposition of solid particulate in this kind of applications is a very long-time process. During this period, the target geometry changes due to the deposition layer growth. On the other hand, the flow field is affected by the modification of the wall boundary, giving a feedback effect on the particle transport as well. Assuming a stationary deposit pattern is only consistent to the beginning of the process, when the target geometry is weakly affected by the growth of deposit layer. Established that a time-marching simulation of the process is unfeasible for the timescales involved in this process, we will simulate it by adopting the technique introduced and applied on erosion problems in [3] and [27]. This method was based on adaptive boundary method and an erosion scale factor. In the present paper, we adopt the same approach, applying it to the study of long-term deposition process on an axial large fan.

In order to improve the quality of the numerical solution we change the aerodynamic model in the algorithm to the finite element RBVMS (Residual-Based Variational Multi Scale) model proposed firstly by Hughes [28]. This model can be coupled with a novel version of the PCT (particle cloud tracking) approach that we propose here. The new formulation can consider also the non-isotropic shape of the Reynolds stress by using an ellipsoidal cloud shape and statistical particle distribution, instead of the original simplified spherical description, correlated with the fine-scales terms of the VMS method.

The algorithm can produce a map of the evolution of the deposit layer on the target (and modification of its boundary) over the count of particles ingested by the fan in its operation. Once field data on the average particle flow-rate is known, it is possible to use it with the obtained map, to scale it and estimate the deposit evolution due to that specific particle flow-rate.

NOMENCLATURE

Latin

C_D	particle drag coefficient
CG	centre of gravity
CoR	coefficient of restitution
d	diameter
e	deposit thickness
E	Young's modulus
g	acceleration of gravity
l.e.	leading edge
K	Kinetic energy
m	mass
p	pressure
$\boldsymbol{r}_{M,}\, r_C$	Navier-Stokes eq. residuals
S	target surface
S	co-variance matrix of the particle distribution in the cloud
t	time abscissa
t.e.	trailing edge
u	fluid velocity vector
v	particle velocity vector
x	Cartesian coordinate vector
y	yield stress

Greek

α	impact angle
δ	relative approach between a particle and the target body
ρ	density
$\boldsymbol{\sigma}$	stress tensor
ν_{LSIC}	stabilization factor

τ_{SUPS} stabilization factor

τ_R cloud relaxation time

τ_L time scale of the particle-laden flow

τ_G turbulence time scale ω model quantity

Γ work of adhesion

Sub-scripts and other symbols

c cloud

f fluid

p particle

h element size reference (coarse scale VMS term)

( )' fine scale term

$\langle\ \rangle$ ensemble average

Acronyms

CFD Computational Fluid Dynamics

PCT Particle Cloud Tracking

PDF Probability Density Function

MaSAI Multiphase Solver and Adaptive-mesh Interface

RB-VMS Residual Based Variational Multi Scale

NUMERICAL TECNIQUE

Main algorithm

We use the same Multiphase Solver and Adaptive-mesh Interface (MaSAI) developed and applied in [3] and [27], adapted to the deposit case. The algorithm is summarized in the flowchart reported in Figure 1. The iteration starts by loading the initial numerical domain and boundary conditions. Then the interface launches the CFD solver to produce the steady flow field. Once the latter is provided, the PCT solver PC-Track starts, considering the flow field as an input to compute the particle transport and possible deposit on the boundary surface. At the end of PC-Track simulation, the deposit distribution throughout the domain is known. Therefore, the algorithm can scale the quantity according to the scale strategy [3], and move the grid nodes as reported in *Deposit thickness* section.

As noticed also for the erosion case [3], for very small changes of the boundary shape, the domain geometry remains virtually identical, and no relevant effects on flow field can be observed. In order to speed up the process, we set a minimum boundary displacement (e_{thr}) to trigger the geometry updating, moving the displacement step from an iteration to another. Below $e_{thr,}$ both the grid and flow field are assumed to be unaffected by the deposit. This allow us to assume that the same CFD and PCT simulation are applicable until the geometry does not update to the next step. Then, at the end of each PC-Track simulation MaSAI evaluates the predicted maximum thickness e_{max} and computes the scale factor F. This last parameter depends on the strategy and on the erosion/deposition model. For this application, the same approach of [3] can be adopted, thus writing $F = \tau = e_{thr}/e_{max}$. *MaSAI* algorithm then multiplies the boundary displacement e by F, forcing at each iteration a maximum value of deposited material always equal to e_{thr}. This leads to an expansion (or possibly a contraction) of the actual simulated particle quantities (and the simulated time as well) at each MaSAI iteration. The erosion displacements of the grid nodes computed as exposed, are then applied and the Adaptive Mesh solver implemented in our FEM code provides a new grid for the eroded geometry. MaSAI is now ready to start a new iteration. Mesh moving is performed adopting the method introduced in [32]-[34], and already used by the authors in [3] and [35].

The result of the described procedure is the deposit evolution on a specific deposit-step size. In this way, it is possible to build a map, which correlates the deposit evolution and the modified configuration with the amount of particle needed to give rise to such a layer. In presence of real field data, this map can be easily scaled using the measured average particles flow-rate, thus obtaining the scaled time map of the process (see *Real field application example* Section for more details).

Aerodynamic Model

We implement the finite element formulation of the RBVMS (Residual-Based Variational Multi Scale) model to simulate the 3D turbulent flow around the fan blade. The original formulation of the model has been firstly proposed by Hughes [28] and Bazilevs [29], and further developed and applied by Tezduyar and Takizawa (e.g., [30]), to the simulation of large set of turbulent flow cases with also moving boundaries.

The main VMS is obtained from the weak stabilized Petrov-Galerkin formulation of the Navier-Stokes equations by splitting the weighting and solution functions spaces into subspaces that contain coarse and fine scales.

This implies that the flow field quantities $\boldsymbol{u}$ and p, in the finite element problem, can be written as

$$\begin{aligned} \boldsymbol{u} &= \boldsymbol{u}^h + \boldsymbol{u}' \\ p &= p^h + p' \end{aligned} \qquad (1)$$

As presented in [31], the fine scales terms can be modeled as follows

$$\begin{aligned} \boldsymbol{u}' &= -\frac{1}{\rho}\tau_{SUPS} r_M(\boldsymbol{u}^h, p^h) \\ p' &= -\rho \nu_{LSIC} r_C(\boldsymbol{u}^h) \end{aligned} \qquad (2)$$

where

$$\begin{aligned} r_M(\boldsymbol{u}^h, p^h) &= \rho\left(\frac{\partial \boldsymbol{u}^h}{\partial t} + \boldsymbol{u}^h \cdot \nabla \boldsymbol{u}^h\right) - \nabla \cdot \boldsymbol{\sigma}(\boldsymbol{u}^h, p^h) \\ r_C(\boldsymbol{u}^h) &= \nabla \cdot \boldsymbol{u}^h \end{aligned} \qquad (3)$$

These terms are very important in our case as we will define a non-spherical distribution of the particle clouds and PDF based on the Reynolds stress terms, which can be directly obtained from these terms (see [29] for further details about the RBVMS model).

All the simulations are then performed using an original parallel Multi-Grid Finite Element flow solver [37], which uses C++ technology and libMesh libraries [38].

Particle tracking and dispersion

Particle trajectories are computed in a Lagrangian reference frame with a one-way dependence between flow and particles [39]. Then, we adopt a PCT approach firstly defined in [40]-[42], and then adapted by the authors to turbomachinery simulations (i.e., [44]-[47]), in order to compute the trajectory of a group of particles (a "cloud"). The cloud equation of motion is given by the Basset-Boussinesque-Oseen formulation, which according to the force analysys carried out by Armenio and Fiorotto [48], reads as

$$\frac{d\boldsymbol{v}_c}{dt} = \tau_R^{-1}\left(\langle \boldsymbol{u} \rangle - \boldsymbol{v}_c\right) + \langle \boldsymbol{f} \rangle + \left(1 - \frac{\rho_f}{\rho_p}\right)\boldsymbol{g} \qquad (4)$$

where < > denotes ensemble average of the enclosed quantity (defined later), $\boldsymbol{f}$ is the centrifugal and Coriolis forces, ρ_p is the particle density, v_c is the cloud velocity, ρ_f is the fluid density, and τ_R is the cloud relaxation time, which, for spherical particles, reads as

$$\tau_R^{-1} = \frac{3}{4 d_p} C_D \frac{\rho}{\rho_p} \left\| \langle \boldsymbol{u} \rangle - \boldsymbol{v}_c \right\| \qquad (5)$$

Here, d_p is the particle diameter and C_D is the drag coefficient in the Shiller and Neumann formulation as reported in [49].

The ensemble average of a given quantity θ within the cloud is defined as

$$\langle \theta \rangle = \frac{\int_{\Omega_c} \theta PDF(\boldsymbol{x}, t) d\Omega}{\int_{\Omega_c} PDF(\boldsymbol{x}, t) d\Omega} \qquad (6)$$

where Ω_c is the cloud domain, and $PDF(\boldsymbol{x},t)$ is the multi-variate probability density function of the dispersed phase.

The PCT approach assumes that particle distribution within a cloud is Gaussian, and the cloud size varies in time according to the properties of the flow. In earlier works ([3],[44]) the Gaussian distribution followed a simplified assumption of spherical clouds and spherical PDF, which means assuming an isotropic and homogeneous turbulence. In that way, the independent variable used to define the PDF distribution was the fluctuation of the cloud radius ($\|\mathbf{x}-\mathbf{x_c}\|$). Since in real situations turbulence is not isotropic nor homogeneous, assuming spherical clouds is reductive. Trying to somehow account for more realistic flow properties, in this work we extend the cloud model to a *nsd*-dimensional shape, considering a joint-normal distribution defined for the set of random variables $\mathbf{x}=\{x_1,...,x_D\}$ with $D = nsd$. This produces a non spherical (namely, ellipsoidal) cloud shape deforming according to turbulence properties of the flow. By definition, the PDF of the joint-normal distribution of the particles within the cloud writes as [50]

$$PDF(\boldsymbol{x},t)=\frac{1}{\sqrt{(2\pi)^{nsd}\,\det(\mathbf{S})}}e^{-\frac{1}{2}\left[(\boldsymbol{x}-\boldsymbol{x}_c)\mathbf{S}^{-1}(\boldsymbol{x}-\boldsymbol{x}_c)\right]} \qquad (7)$$

where **S** is the covariance matrix of particle position, which accounts for the turbulent dispersion of particles.

The dependence of the joint PDF to $\boldsymbol{x}$ is contained in the quadratic form $(\boldsymbol{x}-\boldsymbol{x_c})\mathbf{S}^{-1}(\boldsymbol{x}-\boldsymbol{x_c})$.

For nsd=3, the iso-probability surfaces in the space are ellipsoids, with axes directions defined by the eigenvectors of **S** and axes lengths corresponding to the eigenvalues of **S**. In this way, we can allow the modification of cloud shape with time.

Recalling the definition of fluctuating component of the particle velocity for the cloud, driven by the turbulent dispersion of particles, given in [43]-[46], to obtain the covariance matrix we considered, the definition

$$\left(v_i'\right)_c^2=\left(u_i'\right)_c^2\left(1-e^{\tau_G/\tau_R}\right) \qquad (8)$$

We obtain the covariance matrix, assuming it to be dependent upon the Lagrangian time scale of the particle-laden flow τ_L, and on the Reynolds stress terms as follows

$$\mathrm{S}_{ij}\left(\boldsymbol{x},t\right)=2\sqrt{\left\langle u_i'^2\right\rangle\left\langle u_j'^2\right\rangle}\tau_L^2\left(1-e^{\tau_G/\tau_R}\right)\left[\frac{t}{\tau_L}-e^{-t/\tau_L}\right]+\mathrm{S}_{ij}^{t=0} \qquad (9)$$

where τ_L, is defined as

$$\tau_L=\max\left(\tau_G,\tau_R\right) \qquad (10)$$

At this point, we propose to define τ_G as

$$\tau_G=C_\mu^{3/4}\sqrt{\frac{3}{2}}\max\left(\frac{u_i'^2}{\varepsilon_{ii}}\right) \qquad (11)$$

with $C\mu=0.09$ and ε_{ii} the diagonal components of the dissipation tensor defined in the Reynolds stress transport equation [50].

Then, we adopt the definitions for $(u_i')_c^2$ based on the VMS approach already discussed.

Deposition model

Particle impact and deposition is here modelled using the approach proposed by Thornton and Ning [51]. Starting from the Johnson-Kendall-Roberts theory [52], the impact/adhesion of particles is modelled by computing the coefficient of restitution *CoR* (that is, the ratio between rebound and impact normal velocities, $CoR=v_{r,n}/v_{i,n}$). The variation of kinetic energy ΔK undergone by a particle during an impact with a second body writes

$$\Delta K = \frac{1}{2} m^* v_{r,n}^2 - \frac{1}{2} m^* v_{i,n}^2 \qquad (12)$$

where $m^* = m_1 m_2 / (m_1 + m_2)$ is the equivalent mass, and m_1 and m_2 are the mass of bodies 1 and 2 respectively. This energy variation is due to the detachment of the particle from the target body, and to possible plastic deformations [52]. Therefore, the coefficient of restitution can be expressed in terms of energy dissipation as

$$CoR^2 = 1 - \frac{\Delta K}{\frac{1}{2} m^* v_{i,n}^2} \qquad (13)$$

The case $CoR \leq 0$ means that the particle kinetic energy at the impact equals (or is smaller than) ΔK, thus it is not sufficient to make the particle bounce off the second body ($v_{r,n}=0$), hence it sticks to it. By assuming $CoR=0$, Thornton and Ning computed the sticking velocity v_s, that is the maximum impact velocity at which a particle sticks to the target:

$$v_s = 1.84 \left[\frac{\left(\Gamma / r_p\right)^5}{\left(\rho_p^3 E^{*2}\right)} \right]^{1/6} \qquad (14)$$

being $E^*=E_1E_2/[E_2(1-\upsilon_1^2)+E_1(1-\upsilon_2^2)]$ the equivalent Young modulus, E_1 and E_2 the Young modulus of bodies 1 and 2 in contact, υ_1 and υ_2 the Poisson coefficient of body 1 and 2, respectively. Moreover, it is also possible to compute the minimum impact velocity at which plastics deformations start to take place (yield velocity, v_y)

$$v_y = \left(\frac{\pi}{2E^*} \right)^5 \left(\frac{2}{5\rho_p} \right)^{0.5} y^{2.5}. \qquad (15)$$

According to this, the coefficient of restitution assumes different forms depending on the value of the impact velocity. Namely, Thornoton and Ning computed the following expressions [51]

$$CoR = 0 \qquad for \quad \omega_s \geq 1$$
$$CoR = \left[1-\omega_s^2\right]^{1/2} \qquad for \quad \omega_s < 1 \leq \omega_y \qquad (16)$$
$$CoR = \left\{ 2.078\left[1-\frac{\omega_y^2}{6}\right]\sqrt{\omega_y\left(\omega_y + 2\sqrt{\frac{6}{5}-\frac{1}{5}\omega_y^2}\right)^{-1} - \omega_s^2} \right\}^{\frac{1}{2}} \quad for \ \omega_y < 1$$

being $\omega_s = v_s/v_{i,n}$, $\omega_s = v_y/v_{i,n}$.

Net adhesion energy

An important aspect often neglected when simulating particle deposition is that the net adhesion energy (NEA, eq. (17)), that is the energy required to break the contact between an impacting particle and the target body, varies according to the impact conditions [53].

$$NEA = \int_0^{-\delta_D} F d\delta' = 7.09\left(\frac{R_c^4 \Gamma^5}{E^{*2}}\right)^{\frac{1}{3}} \qquad (17)$$

F is the contact force between the two bodies, δ is the relative approach between the two bodies, D denotes the point at which the contact between the two bodies brakes, and R_c is the radius at contact. The latter quantity varies according to the contact conditions. Namely, while in elastic impacts R_c equals the equivalent radius R^* (18), in elastic-plastic impacts it accounts for the deformation of the particle during the impact, hence resulting in a larger values [53],[54]. Moreover, R_c depends on the radius of the two bodies in contact.

$$\frac{1}{R^*} = \frac{1}{R_1} + \frac{1}{R_2} \qquad (18)$$

R is the radius of the two (1 and 2) bodies in contact. Further details can be found in [49],[50].

Accordingly, if the particle impacts a flat and clean surface, the NEA is that computed by [52] and used in several models (i.e., [51], [54]-[57]). In the case of a particle impacting a partly or totally fouled surface, the particle is not (or not only) into contact with a flat surface but with a number of other particles (Figure 2), and this of course makes the NEA increase. Considering a particle impacting a partially fouled surface (Figure 2-b), and assuming that particles distribute in a regular pattern on the surface, we can say that the impacting particle (the red one in figure) is in contact with the flat surface and with (on average) three already deposited particles. Therefore, the NEA in this case is the sum of that due to the four single contacts. In the case of a particle impacting a surface completely covered by a deposit layer (Figure 2-c), one can assume that (on average) the particle is in contact with six already deposited particles. Thus, the NEA is given by the sum of the NEA of each of these contacts. As a result, the NEA increases as the particles deposit on the surface, which in turn results in an increase of the sticking velocity. As an example, Figure 3 shows the variation of sticking velocity as a function of different impact conditions for 25 μm particles.

Since the deposit information are transported and stored at the domain nodes, in the present study the selection of the proper NEA is done according to the following assumptions:

- if the target surface (limited by four nodes) has less than two nodes containing deposit, each new impacting particle is impacting a clean flat surface
- if the target surface has just three nodes containing deposit, each new impacting particle impacts a partly fouled surface (1st layer case)
- if all the nodes of the target surface contain deposit, then each new impacting particle impacts a totally fouled surface (2nd layer case).

Deposit thickness

The issue of evaluating the deposit thickness e_{dep} is in general complicated by the fact that different particle sizes can deposit simultaneously, resulting in an irregular arrangement. For real industrial applications, it is necessary to use some simplifications and integral modelling. We recall here the approach based on the deposit bulk density ρ_{dep} already used by the authors in former studies (e.g. [53], [58]). The bulk density represents the deposit density comprising the void fraction, thus it accounts for the real particle arrangement in deposit layers.

The evaluation of ρ_{dep} is generally done by experiments. In absence of experimental data, we can estimate ρ_{dep} as

$$\rho_{dep} = \rho_p(1-\varphi)$$

where the porosity factor φ is defined as the ratio between the volumes of the void with respect to the volume of deposit material in a given volume. Considering the approximation of spherical particle of one size class, we assume a particle density of 2000 kg/m^3 and a porosity of φ=0.3, as reported in [58] (Table 1). Such values are typical in ash and soot (that is the main kind of particles in road tunnels) deposition for the considered range of particle size.

Estimation of deposited mass m_{dep} can be done during the PCT simulation. Defining n_p as the number of particles sticking to the surface S, m_p their mass, it writes

$$m_{dep} = n_p m_p \qquad (19)$$

Then, the deposit thickness is:

$$e_{dep} = \frac{m_{dep}}{\rho_{dep} S} \qquad (20)$$

In numerical simulations of particle erosion or deposition, to have statistically independent results the number of simulated particles is usually large but different from the actual situation, and the same is valid for the number of impacting particles n_{pi}. Depending on what type of evolution we want to observe, we should scale this quantity accordingly. Therefore, a further scale factor has to be used, as detailed in sections *Main Algorithm* and *Simulation (Real-simulated data scale mapping)*.

FAN AND OPERATING CONDITION

We built the geometry for this study referring to the characteristics of a large axial fan, used for tunnel and metro ventilation, already presented in [36]. The selected fan has reversible blade with the geometrical characteristics reported in Table 1.

For the computation, we consider the blade installed on the hub with a pitch angle of 20 degrees and processing an average flow rate close to the peak efficiency point [36]. This strong assumption is made in absence of more specific data on a particular duty cycle or installation of the fan. In fact, it simplifies the computation but it does not change the meaning of the study, as the same process can be repeated and refined referring to any point of the fan characteristic curve.

Simulation set-up

A grid of 1.3M of hexahedral elements models the space of a single blade vane. The domain extends for 0.25R upwind and 1.25R downwind (R is the fan radius). The domain characteristics replicate the one used in the study reported in [36], where it is possible to find a validation of the numerical solution with respect to the real fan data.

Figure 5 shows the domain on the blade relative reference frame, where Z is the blade axis and Y is the rotor axis. All the simulations are performed on this non-inertial rotating frame.

The inlet and outlet boundary conditions equal 80 m^3/s of flow rate. Wall functions are applied to the hub, while the equations are integrated at the wall for the blade and case surfaces. Periodicity is imposed at the last two sides. The grid has built to show $y+<1$ at the wall with no-slip boundary conditions. The fluid phase is composed of air at 20 °C.

For the PCT solver, we simulate an array of five clouds containing 50M of particles each.

Cloud mean positions enter the domain from five different elements located on the line in which the streamlines directed to the blade leading edge starts from the boundary surface. Particle diameter used for the computation equals 10 µm, with main characteristics reported in Table 1.

The evolution simulation has been carried on, in this phase of the work, for six iterations imposing e_{thr} = 0.25 mm.

RESULTS

Deposit evolution

Figure 6 shows the step-by-step values of the maximum local impact number on the blade, and of the maximum deposited mass per unit surface, both values computed in the PCT simulation. The configuration corresponding to the fifth iteration produces a larger concentration of the deposit. However, we can observe that the order of magnitude of the maximum is always the same. The difference observed in the fifth point can be due to a slightly different aerodynamic field, proving that the coupled flow/particle transport systems are sensible to any variation of the boundary shape. Indeed, adhesion is related to local values of the impact angle and impact velocity, both depending on the local surface normal (changing from step to step due to deposit) and flow field dynamics (affected by the modification of the blade surface). Therefore, a localized change of the surface normal due to the deposit, results in a better or worse adhesion capability of the particle flow in the considered location. This mechanism is intrinsically non-linear and unpredictable a-priori, proving again that the use of an evolution algorithm is necessary to simulate correctly this class of problems.

The impact number per unit surface reflects this trend. This is not always true as shown for the erosion case presented in [3]. The motivation comes from the location where this value is registered. In our case, it corresponds to the blade leading edge in all the simulations. This aspect can be observed in Figure 7 that shows the evolution of the boundary line at the leading edge. The figure points out the non-linear nature of the process. Indeed, even for very similar deposit distribution and aerodynamic fields (as will be evident in the next section), the growth of the deposit layer is non-linear and changes its local shape at every iteration, as effect of the change in aerodynamic field around the blade. As shown, deposit is slightly M-shaped (red dashed line in Figure 7), having the minimum close to the stagnation point and the maxima at its sides. This is in agreement with what found in a previous study by some of the authors [53]. As demonstrated in that study the M-shape is related to the particle size (and Stokes number): the larger is the size the less evident is this shape.

Figure 8 shows the deposit contour on the blade surface, for the first and last step, and the trajectories of the clouds centres of mass. From the trajectories of the clouds we can observe how the aerodynamic field push them toward the mid-sections of the blade. No visible effects on the trajectories seem to be present on cloud trajectories if comparing the first and the last step, but actually some small differences are present. However, the shape of the deposit shows some differences

.the main deposit concentration areas are in direct correlation with the shape of the aerodynamic field, as will be shown and explained in the next session.

In Table 2 we report the value of scale factors corresponding to each evolution step, and used to scale the particle count and displacement to the value needed to obtain the given boundary displacement threshold.

Effect on the aerodynamic field

The effect on the aerodynamic field is firstly measurable though the fan performance. Figure 9 shows their progressive variation in terms of pressure jump losses. We notice an increasing loss in performance associated to the deposit layer evolution. The trend is non linear and, as observed in [3] and confirmed by Figure 9, it is possible to find that a configuration of the blade with more deposit (e.g. iteration 6) has less detrimental effect on the aerodynamic field with respect to the former ones (with less overall deposit accumulation).

From Figure 9 it would be possible to identify the performance damage (and the blade deposit configuration) at a given operational time, by scaling the particle count axis with a given real field particle flowrate. An example of this passage will be given in the next section.

Figure 10 shows a sketch of the aerodynamic field (in terms of vortex structures and pressure field) corresponding to the first and last steps of the evolution. It is possible to notice how the aerodynamic field is divided in three main areas: a strong tip vorticity, a less perturbed field in the midspan sections, and a strong root vorticity around the trailing edge side of the blade root sections. These three structures affect the shape of the deposit on the blade surface (Figure 8). The recirculation at the root produces the accumulation of particle deposit along the line of vortices downwash. In a different manner, the tip vorticity and high turbulence and energy flow around the tip of the blade, blow the particle clouds down (Figure 8), resulting in a less amount of deposit in this region. We can observe this behaviour in all the steps as it is related to the normal working condition of the blade. At the midspan, the most affected area (also location of the maximum value of deposit on the blade) is the leading edge.

Real field application example

Knowing a measured particle concentration (or volume-rate), it is possible to scale the simulation data over an equivalent time, by combining the actual flow-rate with the simulated scaled particle counts. In this case, we apply the measurement reported in [59]. In that study, the average particle concentration of coarse $PM_{2.5\text{-}10}$ has been measured at the centre of a freeway tunnel in southern Taiwan. The reported value is a concentration C = 24μg/m^3 of particles. Considering this concentration and assuming that all particles have the same size (i.e., 10 μm), it is possible to convert the number of scaled particles corresponding to each evolution step into number of hours.

First, we can approximate that the inflow velocity of the particles equals the air inflow velocity (see Table 1). In this way, the particle flowrate writes

$$\dot{n}_{\text{inf}} = C\dot{m} = 1833465 s^{-1} \quad (21)$$

Therefore, we can obtain the equivalent hours by dividing the scaled number of particle of Figure 9 by the particle average flow rate, obtaining the results reported in Table 3. With the assumption adopted, the six evolution steps are equivalent to about 3200 fan operating hours.

CONCLUSION

We presented the simulation of the deposit evolution on a large axial fan for tunnel ventilation.

The analysis is performed assuming 10 µm particles, a size class commonly present in the road tunnel atmosphere.

The integrated algorithm adopted in the study uses a steady aerodynamic field obtained through a RBVMS finite element formulation, to predict the transport and morphing of ellipsoidal clouds of particles. The particle cloud approach has been upgraded to account for the anisotropic nature of the turbulent flow. Then, the displacement thickness is computed and scaled on the base of a user-defined threshold value. After the computation, the thickness of deposit layer is used to move the boundary of the domain and the domain internal nodes. The algorithm has repeated this procedure iteratively for 6 times. The result is a map that correlates the deposit on the blade with particle load processed by the fan inflow. This final map can be scaled on any real field measurement of particles concentration to obtain the time evolution. As example, we took from literature a field measurement of particle concentration in a road tunnel in Taiwan, to scale the result and obtain an equivalent time abscissa for the 6 deposit evolution steps. On this particular case, the simulation was equivalent to 3200 hours of work at the chosen operating condition, predicting a thickness of the deposit layer at the leading edge of around 0.6 mm and a drop of pressure jump of around 5%.

REFERENCES

[1]. Sheard AG, Corsini A., The impact of an anti-stall stabilisation ring on industrial fan performance: implications for fan selection. InASME 2011 Turbo Expo: Turbine Technical Conference and Exposition 2011 Jan 1 (pp. 311-323). American Society of Mechanical Engineers.

[2]. A. Corsini, G. Delibra, A.G. Sheard, A Critical Review of Computational Methods and Their Application in Industrial Fan Design, ISRN Mechanical Engineering, 2013, article ID 625175.

[3]. Castorrini, A., Venturini, P., Corsini, A., Rispoli, F. (2019). Numerical simulation of the blade aging process in an induced draft fan due to long time exposition to fly ash particles. Journal of Engineering for Gas Turbines and Power, 141(1), 011025.

[4]. Castorrini, A., Corsini, A., Rispoli, F., Venturini, P., Takizawa, K., & Tezduyar, T. E. (2019). Computational analysis of performance deterioration of a wind turbine blade strip subjected to environmental erosion. Computational Mechanics, 1-21.

[5]. Corsini, A., Rispoli, F., Sheard, A.G., Venturini, P. (2013), Numerical simulation of coal fly-ash erosion in an induced draft fan, ASME Journal of Engineering for Gas Turbine and Power, vol. 135 (8), article no. 081303.

[6]. A. Corsini, A. Marchegiani, F. Rispoli, P. Venturini, A.G. Sheard, Predicting blade leading edge erosion in an axial induced draft fan, ASME Transactions, Journal of Engineering for Gas Turbine and Power (ISSN:0742-4795), 2012;134(4), article no. 042601.

[7]. Cardillo L., Corsini A., Delibra G., Rispoli F., Sheard A.G., Venturini P., Simulation of particle-laden flows in a large centrifugal fan for erosion prediction, ASME Turbo Expo 2014, Dusseldorf, Germany, paper no. GT2014-25865.

[8]. L. Cardillo, A. Corsini, D. Borello, G. Delibra, A. Salvagni, F. Rispoli, P. Venturini, Modelling of particle transport, erosion and deposition in power plant gas paths, Turbo Expo 2016, Seul, South Korea, 13-17 June, 2016, paper no. GT2016-57984.

[9]. Y. Wang, H. Tan, K. Dong, H. Liu, J. Xiao, J. Zhang (2017), Study of ash fouling on the blade of induced fan in a 330 MW coal-fired power plant with ultra-low pollutant emission, Applied Thermal Engineering, vol. 118, pp. 283-291.

[10]. Van Der Spuy, S.J., Von Backström, T.W., Kröger, D.G. (2011), Using computational fluid dynamics to simulate multiple axial flow fans in air-cooled steam condensers, ASME Power Conference 2011, 12-14 July, Denver, Colorado, paper no. 98549.

[11]. Louw, F.G., Von Backström, T.W., Van Der Spuy, S.J. (2015), Lift and drag characteristics of an air-cooled heat exchanger axial flow fan, ASME Journal of Fluids Engineering, Vol. 137(8), Article number 081101.

[12]. Louw, F.G., Von Backström, T.W., Van Der Spuy, S.J. (2015), Experimental investigation of the blade surface pressure distribution in an axial flow fan for a range of flow rates, ASME Turbo Expo 2015, 15-19 June, Montreal, Canada, paper no. 113665.

[13]. C.P. Bowen, N.D. Libertowski, M. Mortazavi, J.P. Bons (2018), Modeling deposition in turbine cooling passages with temperature dependent adhesion and mesh morphing, ASME Turbo Expo 2018, 11-15 June, Oslo, Norway, paper no. GT2018-76251.

[14]. J.P. Bons, R. Prenter, S. Whitaker (2017), A simple physics-based model for particle rebound and deposition in turbomachinery, Journal of Turbomachinery, vol. 139, article no. 081009.

[15]. S.M. Whitaker, J.P. Bons (2018), An improved particle impact model by accounting for rate of strain and stochastic rebound, ASME Turbo Expo 2018, 11-15 June, Oslo, Norway, paper no. GT2018-77158.

[16]. Yu, K., Tafti, D. (2017), Size and temperature dependent deposition model of micro-sized sand particles, ASME Turbo Expo 2017, 26-30 June, Charlotte, North Carolina, paper no. GT2017-130041.

[17]. Singh, S., Tafti, D. (2015), Particle deposition model for particulate flows at high temperatures in gas turbine components, International Journal of Heat and Fluid Flow, vol. 52, pp. 72-83.

[18]. Singh, S., Tafti, D. (2013), Predicting the coefficient of restitution for particle wall collisions in gas turbine components, ASME Turbo Expo 2013, 3-7 June, San Antonio, Texas, paper no. GT2013-95623.

[19]. P. Forsyth, D. Gillespie, M. McGilvray (2017), development and applications of a coupled particle deposition dynamic mesh morphing approach for the numerical simulation of gas turbine flows, ASME Turbo Expo 2017, 26-30 June, Charlotte, North Carolina, paper no. GT2017-63295.

[20]. J. Connolly, P. Forsyth, M. McGilvray, D. Gillespie (2018), The use of fluid-solid cell transoformation to model volcanic ash deposition within a gas turbine hot component, ASME Turbo Expo 2018, 11-15 June, Oslo, Norway, paper no. GT2018-76683.

[21]. N. Casari, M. Pinelli, A. Suman (2018), On deposition and build-up detachment in compressor fouling, ASME Turbo Expo 2018, 11-15 June, Oslo, Norway, paper no. 138886.

[22]. N. Aldi, N. Casari, D. Dainese, M. Morini, M. Pinelli, P.R. Spina, A. Suman (2018), Fouling on a multistage axial compressor in the presence of a third substance at the particle/surface interface, ASME Turbo Expo 2018, 11-15 June, Oslo, Norway, paper no. 138886.

[23]. D. Borello, F. Rispoli, P. Venturini, An integrated particle-tracking impact/adhesion model for the prediction of fouling in a subsonic compressor, Journal of Engineering for Gas Turbine and Power, 2012;134(9).

[24]. G. Agati, D. Borello, F. Rispoli, A. Salvagni, P. Venturini, Numerical simulation of a particle-laden impinging jet: effect of wall curvature on particle deposition, Turbo Expo 2017, Charlotte, North Carolina, 26-30 June, 2017, paper no. GT2017-64629.

[25]. Borello D., D'Angeli L., Salvagni A., Venturini P., Rispoli F., Study of particle deposition in gas turbine blades in presence of film cooling, ASME Turbo Expo 2014, Dusseldorf, Germany, paper no. GT2014-26250.

[26]. F. Birello, D. Borello, P. Venturini, F. Rispoli, Modelling of deposit mechanisms around the stator of a gas turbine, ASME Turbo Expo 2013, paper no. GT2013-95688, San Antonio, Texas, June 3-7, 2013.

[27]. Castorrini, A., Corsini, A., Morabito, F., Rispoli, F., & Venturini, P. (2017, June). Numerical simulation with adaptive boundary method for predicting time evolution of erosion processes. In ASME Turbo Expo 2017: Turbomachinery Technical Conference and Exposition (pp. V02DT48A019-V02DT48A019). American Society of Mechanical Engineers.

[28]. Hughes, T. J. (1995). Multiscale phenomena: Green's functions, the Dirichlet-to-Neumann formulation, subgrid scale models, bubbles and the origins of stabilized methods. Computer methods in applied mechanics and engineering, 127(1-4), 387-401.

[29]. Bazilevs, Y., Calo, V. M., Cottrell, J. A., Hughes, T. J. R., Reali, A., & Scovazzi, G. (2007). Variational multiscale residual-based turbulence modeling for large eddy simulation of incompressible flows. Computer Methods in Applied Mechanics and Engineering, 197(1-4), 173-201.

[30]. Takizawa, K., Spielman, T., & Tezduyar, T. E. (2011). Space–time FSI modeling and dynamical analysis of spacecraft parachutes and parachute clusters. Computational Mechanics, 48(3), 345.

[31]. Bazilevs, Y., Takizawa, K., & Tezduyar, T. E. (2013). Computational fluid-structure interaction: methods and applications. John Wiley & Sons.

[32]. Tezduyar T.E., Behr M., Mittal S., Johnson A.A., 1992, Computation of unsteady incompressible flows with the finite element methods – space–time formulations, iterative strategies and massively parallel implementations, New Methods in Transient Analysis, PVP-Vol.246/AMD-Vol.143, ASME, New York, pp. 7–24.

[33]. Tezduyar T., Aliabadi S., Behr M.,1993, A. Johnson, and S. Mittal, 1993, Parallel finite-element computation of 3D flows, Computer, vol. 26, pp. 27–36.

[34]. Johnson A.A., Tezduyar T.E., 1994, Mesh update strategies in parallel finite element computations of flow problems with moving boundaries and interfaces, Computer Methods in Applied Mechanics and Engineering, vol. 119, pp. 73–94.

[35]. Castorrini, A., Corsini, A., Sheard, A. G., & Rispoli, F. (2016, June). Numerical study on the passive control of the aeroelastic response in large axial fans. In ASME Turbo Expo 2016: Turbomachinery Technical Conference and Exposition (pp. V001T09A010-V001T09A010). American Society of Mechanical Engineers.

[36]. Castorrini, A., Corsini, A., Sheard, A. G., & Rispoli, F. (2018). Numerical Testing of a Trailing Edge Passive Morphing Control for Large Axial Fan Blades. Journal of Engineering for Gas Turbines and Power, 140(3), 032606.

[37]. Borello D., Corsini A., Rispoli F., 2003, A finite element overlapping scheme for turbomachinery flows on parallel platforms, Computers and Fluids, 32/7, 1017-1047

[38]. Kirk B.S., Peterson J.W., Stogner, R.,H., Carey, G.,F., 2006, libMesh: A C++ Library for Parallel Adaptive Mesh Refinement/Coarsening Simulations, Engineering with Computers, 22, 237-254

[39]. Rispoli, F., Delibra, G., Venturini, P., Corsini, A., Saavedra, R., & Tezduyar, T. E. (2015). Particle tracking and particle–shock interaction in compressible-flow computations with the V-SGS stabilization and YZ\beta YZβ shock-capturing. Computational Mechanics, 55(6), 1201-1209.

[40]. Baxter L.L., 1989, Turbulent transport of particles. *Ph.D. thesis*, Brigham Young University, Provo, UT.

[41]. Wang L.P, 1990, On the dispersion of heavy paricles by turbulent motion, *Ph.D. thesis*, Washington State University, Pullman, WA.

[42]. Litchford L.J., Jeng S.M., 1991, Efficient statistical transport model for turbulent particle dispersion in sprays, *AIAA Journal*, 29, 1443.

[43]. Smith, P. J. (1991). 3-D turbulent particle dispersion submodel development. DOE Quarterly Progress Report #4, US; 1992 .

[44]. A. Castorrini, A. Corsini, F. Rispoli, P. Venturini, K. Takizawa, T.E. Tezduyar, 2016, Computational analysis of wind-turbine blade rain erosion, Computers and Fluids, vol. 141, pp. 175–183.

[45]. Castorrini A., Corsini A., Rispoli F., Venturini P., Takizawa K., Tezduyar T.E., 2016, SUPG/PSPG computational analysis of rain erosion in wind-turbine blades, Modelling and Simulation in Science, Engineering and Technology, pp. 77-96.

[46]. Castorrini, A., Corsini, A., Rispoli, F., Venturini, P., Takizawa, K., & Tezduyar, T. E. (2016). SUPG/PSPG computational analysis of rain erosion in wind-turbine blades. In Advances in Computational Fluid-Structure Interaction and Flow Simulation (pp. 77-96). Birkhäuser, Cham.

[47]. Corsini, A., Castorrini, A., Morei, E., Rispoli, F., Sciulli, F., & Venturini, P. (2015, June). Modeling of rain drop erosion in a multi-MW wind turbine. In ASME Turbo Expo 2015: Turbine Technical Conference and Exposition (pp. V009T46A001-V009T46A001). American Society of Mechanical Engineers.

[48]. Armenio V , Fiorotto V., The importance of the forces acting on particles in turbulent flows. Phys Fluids 2001;13:2437–40.

[49]. Sommerfeld M., van Wachem B., Oliémans R., 2009, Dispersed turbulent multi-phase flow. Best practice guidelines, ERCOFTAC.

[50]. Pope, S. B. (2001). Turbulent flows.

[51]. Thornton C., Ning Z. (1998), A theoretical model for stick/bounce behaviour of adhesive, elastic-plastic spheres, Powder Technology, 99, 154-162.

[52]. Johnson K.L., Kendall K., Roberts A.D. (1971), Surface Energy and the contact of elastic solids, Proc. of Royal Society of London, series A 324, 301-313.

[53]. P. Venturini, 2010, Particle-wall interaction in two-phase gas-solid flows, Ph.D. Dissertation, Sapienza University of Rome, Italy.

[54]. M.C. van Beek. Gas-side fouling in heat-recovery boilers. Ph.D. Technische Uni-versiteit Eindhoven, Germany, 2001.

[55]. L.N. Rogers, J. Reed. The adhesion of particles undergoing an elastic-plastic with a surface. Journal of Physics D: Applied Physics (1983), 17, 677-689.

[56]. G. Agati, D. Borello, F. Rispoli, P. Venturini (2016), A new approach to model temperature influence on particle deposition in gas turbines, AMSE Turbo Expo 2016, 13-17 June, Seoul, South Korea, paper no. GT2016-57997.

[57]. G. Agati, D. Borello, F. Rispoli, A. Salvagni, P. Venturini, Numerical simulation of a particle-laden impinging jet: effect of wall curvature on particle deposition, Turbo Expo 2017, Charlotte, North Carolina, 26-30 June, 2017, paper no. GT2017-64629.

[58]. Venturini, P., Borello, D., Hanjalić, K., Rispoli, F. (2012). Modelling of particles deposition in an environment relevant to solid fuel boilers. Applied Thermal Engineering, 49, 131-138.

[59]. Hung-Lung, C., Yao-Sheng, H. (2009). Particulate matter emissions from on-road vehicles in a freeway tunnel study. Atmospheric Environment, 43(26), 4014-4022.

TABLES AND FIGURES

Table 1. Geometry and simulation data.

Fan rotor	
Blade number	16
Hub-to-casing diameter ratio	0.357
Tip diameter (mm)	2240
Rotor tip clearance (% span)	1.25
Rated rotational frequency (rpm)	985
Blade tip chord (mm)	210
Blade root chord (mm)	260
Fluid phase	
Fan flow rate (m^3/s)	*80*
Density (kg/m^3)	*1.225*
Viscosity (Pa s)	*$1.81 \cdot 10^{-5}$*
Solid phase	
Density (kg/m^3)	*2000*
Diameter (µm)	*10*
Deposit porosity	*0.3*

Table 2. Scale factor.

Evolution step	*Scale factor*
1	7.96E+02
2	8.81E+02
3	9.32E+02
4	9.83E+02
5	5.81E+02
6	1.10E+03

Table 3. Scaled time of exposition to the particle concentration given in [59].

Evolution step	*Scaled time of operation [hours]*
1	482
2	1016
3	1581
4	2177
5	2529
6	3198

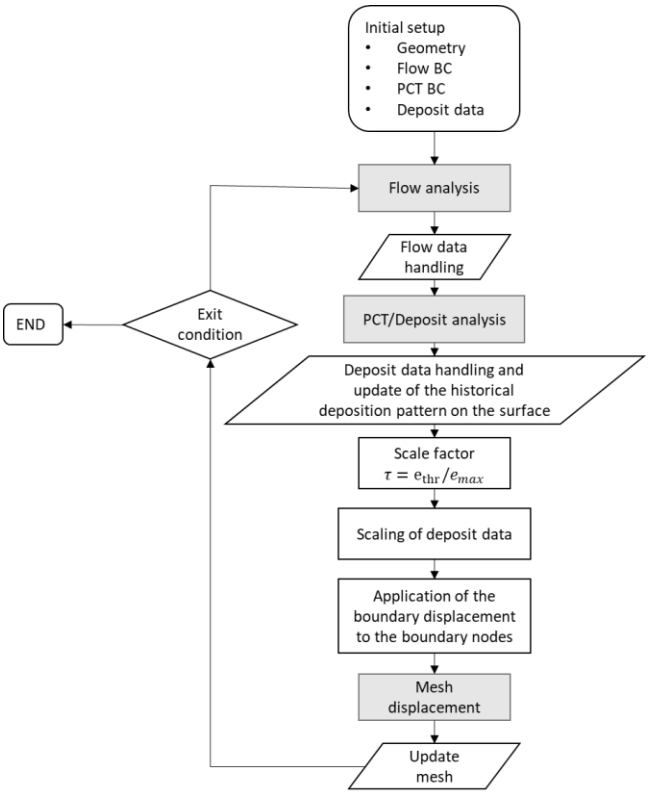

Figure 1. Rationale of MaSAI algorithm.

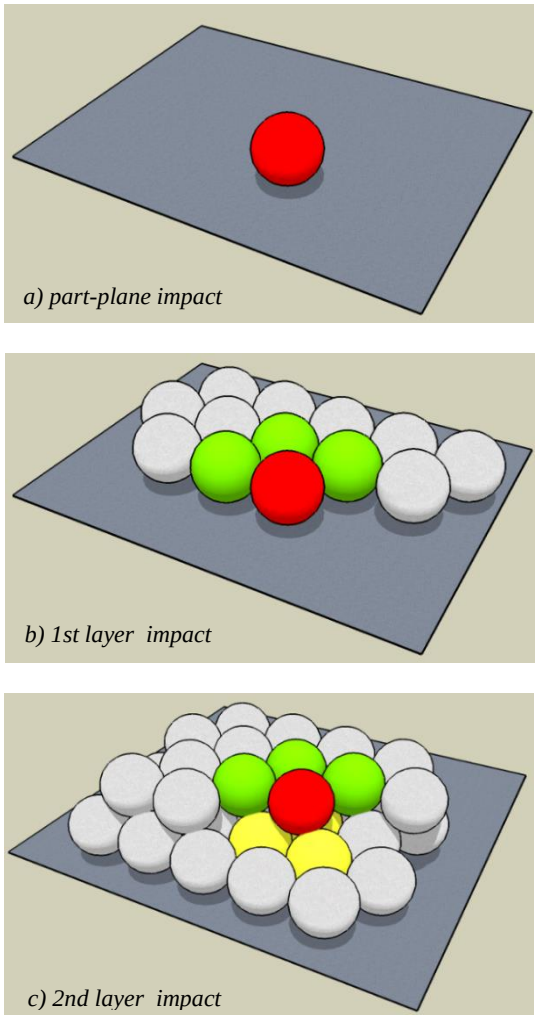

Figure 2. Schematic representation of particle impacting a surface at different condition: a) clean surface; b) partly fouled surface; c) totally fouled surface. Red particle: impacting particle [53].

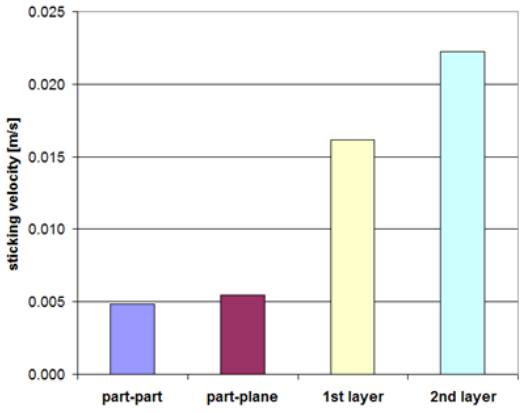

Figure 3. Sticking velocity in different type of impacts, for a 25 µm impacting particle: impact between two particles (part-part), impact on a clean flat surface (part-plane), impact on a partly fouled surface (1st layer), impact on a totally fouled surface (2nd layer) [53].

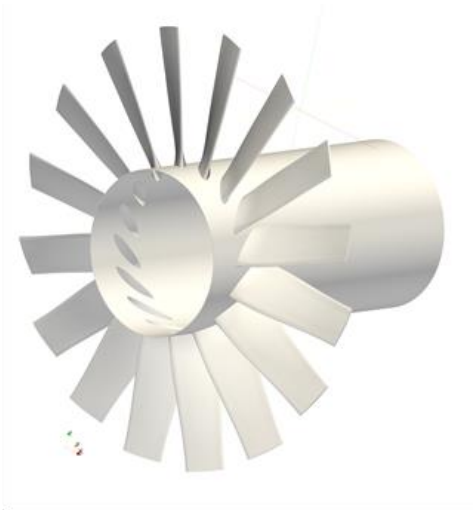

Figure 4. 3D view of the fan CAD model, without the casing.

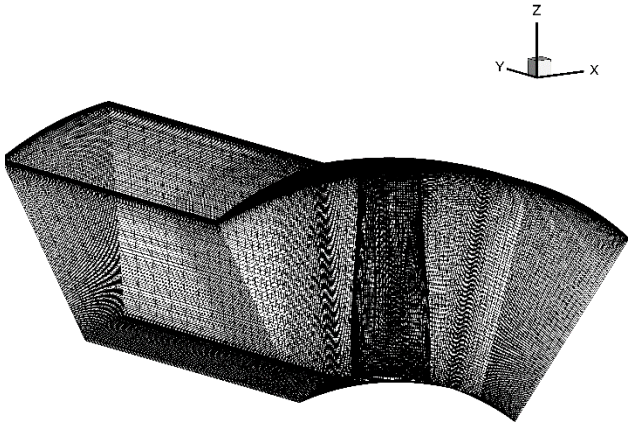

Figure 5. Numerical domain: mesh.

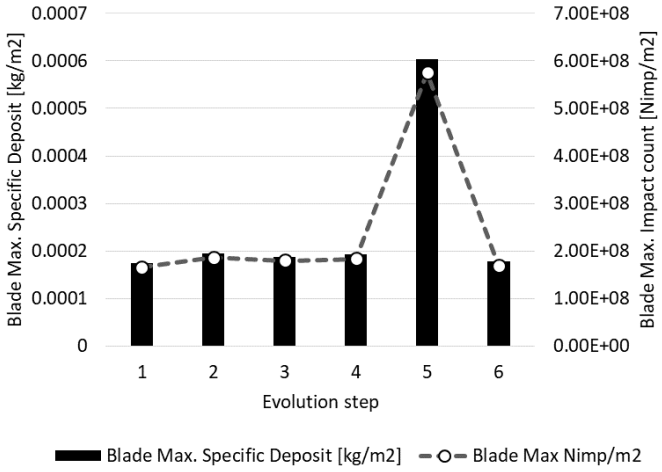

Figure 6. Variation of maximum number of impacting particles per unit surface (top), erosion rate per unit surface (bottom).

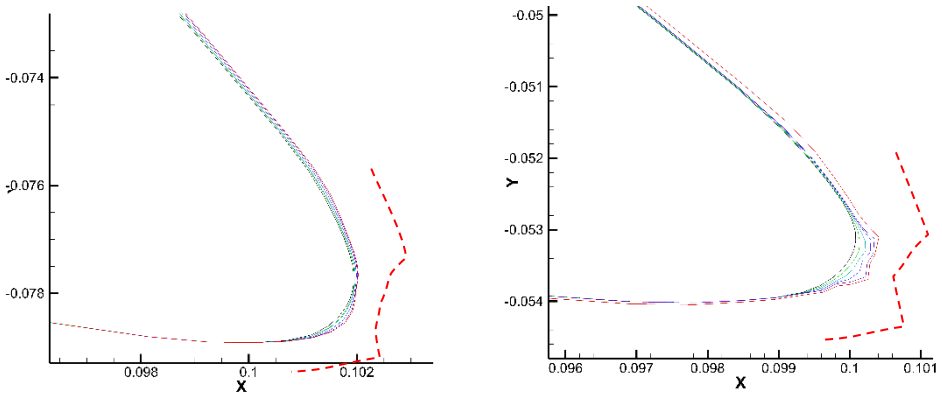

Figure 7. Leading edge shape evolution after deposit step. Top: Section at R=0.83m. Bottom: section at R=0.56m. Red dashed-line: M-shape.

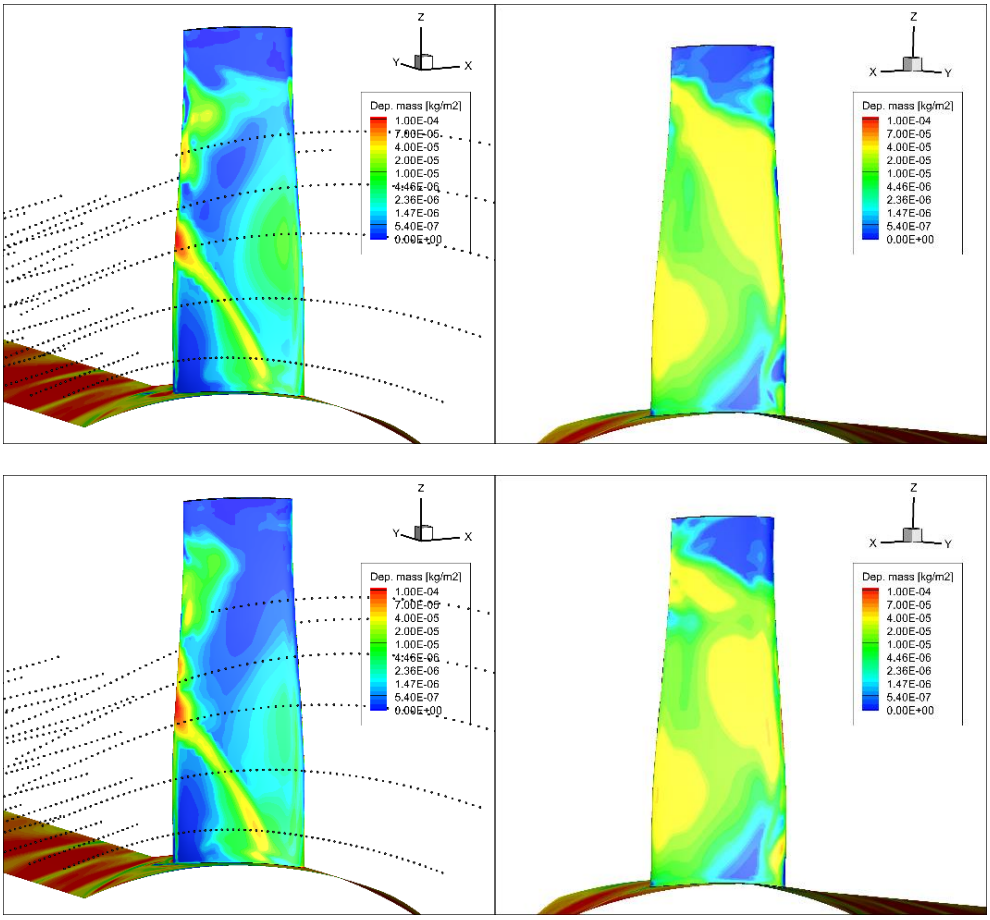

Figure 8. Deposited mass per unit surface at the end of the first (up) and last (down) iterations: suction side (left), pressure side (right).

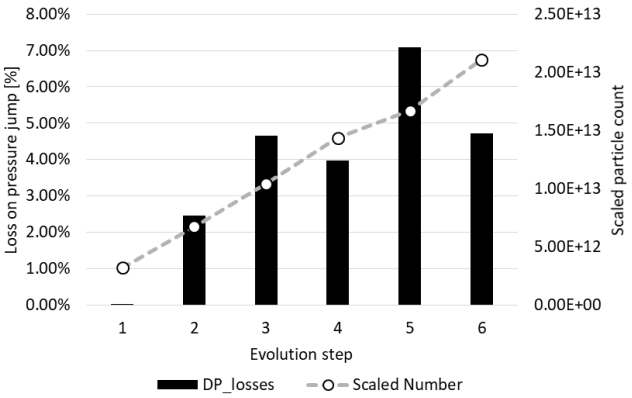

Figure 9. Pressure jump and scaled particle amount variation.

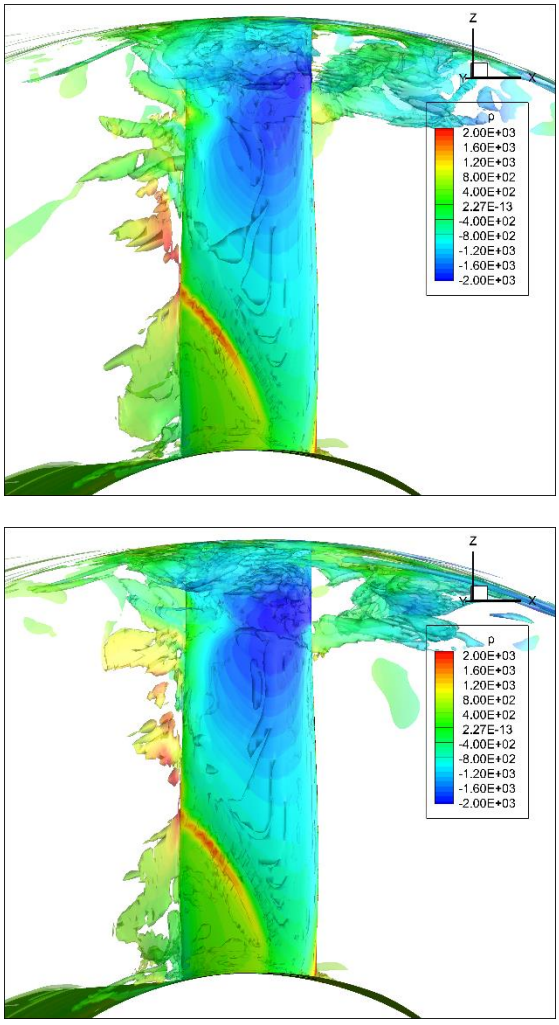

Figure 10. Swirl iso-surfaces and pressure field on the blade suction side, for the first (top) and last (bottom) steps.